JGR Space Physics

RESEARCH ARTICLE
10.1029/2021JA030079

Asymmetric Interaction of a Solar Wind Reconnecting Current Sheet and Its Magnetic Hole With Earth's Bow Shock and Magnetopause

Hadi Madanian[1,2], Terry Z. Liu[3], Tai D. Phan[4], Karlheinz J. Trattner[1], Tomas Karlsson[5], and Michael W. Liemohn[6]

[1]Laboratory for Atmospheric and Space Physics, University of Colorado, Boulder, CO, USA, [2]Space Science and Engineering Division, Southwest Research Institute, San Antonio, TX, USA, [3]University of California Los Angeles, Los Angeles, CA, USA, [4]Space Sciences Laboratory, University of California, Berkeley, CA, USA, [5]KTH Royal Institute of Technology, Stockholm, Sweden, [6]Department of Climate and Space Sciences and Engineering, University of Michigan, Ann Arbor, MI, USA

Abstract We report results of our multi-spacecraft analysis of a solar wind reconnecting current sheet (RCS) and its solar wind magnetic hole (SWMH) observed on November 20, 2018. In the solar wind, the normal vector to the current sheet plane makes an angle of 32° with the Sun-Earth line. A combination of tilted current sheet plane and foreshock effects cause an asymmetric interaction with the bow shock, in which the structure arrives at the quasi-perpendicular side of the bow shock before the quasi-parallel side. The magnetic field strength inside the magnetic hole decreases by ~69 percent in the solar wind, with a similar depression rate observed inside the magnetosheath due to this structure. The solar wind flow slowdown and deflection during the bow shock crossing significantly disrupt the reconnection exhausts within the RCS. The interaction of the RCS and SWMH with the bow shock creates enhanced fluxes of accelerated electrons and ions. Plasma flow deflection in the magnetosheath also increases with the passage of the RCS. The ion density and temperature both increase within the current sheet to form a roughly pressure balanced structure. Field rotation and change in the dynamic pressure during this event modify the reconnection zones at the magnetopause and cause asymmetric inward motions in portions of the bow shock and the magnetopause boundaries (i.e., deformation). Unlike localized magnetosheath jets, an RCS and its associated SWMH in the solar wind have a global impact on the bow shock and the magnetopause.

Plain Language Summary Space Weather is the study of effects of solar inputs on the space environment surrounding Earth. A source of solar input is through the solar wind, a stream of charged particles from the Sun carrying the interplanetary magnetic field. In this study, we analyze effects of a particular type of solar wind anomaly on Earth. The structure is initially observed by solar wind monitors far upstream of Earth, and later appears in the data of several near Earth spacecraft. We show that the structure can pass through the outer most boundary around Earth, the bow shock, and propagate closer to Earth. This study has significance in shaping our understanding of space weather as it describes near-Earth effects of a commonly observed solar wind phenomenon.

Key Points:

- Asymmetric interaction is caused by the current sheet plane orientation in the solar wind and foreshock effects
- Flux of accelerated electrons and ions increase in the magnetosheath due to current sheet and magnetic hole interactions at the bow shock
- The structure causes deformation of the bow shock and magnetopause boundaries and modulates the reconnection process at the magnetopause

Supporting Information:

Supporting Information may be found in the online version of this article.

Correspondence to:

H. Madanian,
hmadanian@gmail.com

Citation:

Madanian, H., Liu, T. Z., Phan, T. D., Trattner, K. J., Karlsson, T., & Liemohn, M. W. (2022). Asymmetric interaction of a solar wind reconnecting current sheet and its magnetic hole with Earth's bow shock and magnetopause. *Journal of Geophysical Research: Space Physics*, *127*, e2021JA030079. https://doi.org/10.1029/2021JA030079

Received 26 OCT 2021
Accepted 31 MAR 2022

1. Introduction

Reconnection has been widely studied and observed in various space plasma environments such as solar flares, the solar wind, Earth's magnetotail and magnetopause (Gosling, 2012; Hesse & Cassak, 2020; Khotyaintsev et al., 2019; Paschmann et al., 2013; Treumann & Baumjohann, 2013; Yamada et al., 2010; Zweibel & Yamada, 2016, and references therein). During reconnection, the magnetic field morphology at the intersection of two rather different plasma environments change in order to diffuse the energy of opposing flows. In the solar wind, a reconnecting current sheet (RCS) is characterized by a rotation in the IMF accompanied by Alfvénic accelerated plasma flows also known as reconnection exhausts (Gosling et al., 2005). Alfvénic disturbances generated during reconnection propagate along reconnected magnetic field lines and accelerate and heat the plasma along their way. For a spacecraft that is relatively stationary in the supersonic solar wind flow, such a structure will appear as correlated changes in the magnetic field (**B**) and the plasma velocity (**V**) on one side, and anti-correlated changes on the other side of the reconnection exhaust. The current sheet can appear

as back-to-back rotational discontinuities (i.e., a bifurcated current sheet) or as a single current sheet (Gosling & Szabo, 2008; Phan et al., 2006, 2009). The physical processes that initiate reconnection are not well determined. A few models describe the scaling relation between plasma parameters during reconnection (Cassak & Shay, 2007; Parker, 1957; Petschek, 1964). Theoretical studies suggest that in the solar wind, compression of the sectored solar wind flow can lead to reconnection (Drake et al., 2017). Reconnection can also be initiated spontaneously. Transfer of magnetic energy to particles creates a magnetic depression or a magnetic hole at the reconnection site. The level of depression varies with distance to the X-line of an expanding exhaust. Energy release during reconnection is also a source of free energy that drives further plasma instabilities causing turbulence in the magnetic field and plasma flow near the reconnection zone (Osman et al., 2014).

Interaction of transient solar wind structures with Earth's bow shock and magnetosphere has been the topic of many investigations. It has been shown that sudden changes in the IMF direction across rotational discontinuities (RDs) can alter the energy input and reconnection rate at the magnetopause, and modify the solar wind-magnetosphere-ionosphere coupling (Andreeova et al., 2011; Liemohn & Welling, 2016; Tsurutani et al., 2011). Archer et al. (2012) showed that some RDs travel in the magnetosheath in the form of pressure pulsations. Change of shock geometry from quasi-perpendicular to quasi-parallel allows for high-pressure plasma parcels to form at certain regions downstream of the shock. Conventionally, magnetosheath "high-speed" jets are known to have a characteristically high velocity component along the magnetopause normal vector that gives rise to the enhanced dynamic pressure (Escoubet et al., 2020; Hietala & Plaschke, 2013; Plaschke et al., 2013). However, high plasma density anomalies in the magnetosheath can also produce high dynamic pressure magnetosheath structures (Blanco-Cano et al., 2020). It has also been shown that compression of the current sheet across solar wind discontinuities at the bow shock can initiate reconnection (Hamrin et al., 2019; Lin, 1997; Phan et al., 2007), as does the compression of current sheets at the magnetopause (Hietala et al., 2018). Current sheet thinning, high magnetic shear angle, and small difference in plasma β between the two plasma environments are favorable conditions for reconnection (Paschmann et al., 1982; Phan et al., 2010).

Bow shock and foreshock environments also significantly modify the current density within RDs (Kropotina et al., 2021). Crossing the bow shock can disrupt the reconnection exhausts and shut off the reconnection process within the RCS (Phan et al., 2011). In some cases, density increase within upstream discontinuities generates a fast shock that propagates in front of the discontinuity in the magnetosheath (Maynard et al., 2008). Due to pressure variations and rarefaction effects, interplanetary shocks induce a rocking motion in the bow shock layer when they cross it (Šafránková et al., 2007). Once inside the magnetosheath, interplanetary shocks take the form of a discontinuity (Zhang et al., 2009). Bow shock crossing also significantly modifies the structure of magnetic clouds, plasma events associated with interplanetary coronal mass ejections and characterized by enhancements in the magnetic field strength during slow field rotations (Farrugia et al., 1995; Turc et al., 2016). Another widely observed transient solar wind phenomenon are magnetic holes (MHs; Turner et al., 1977), characterized as sudden decreases in the magnetic field strength in an otherwise unperturbed solar wind flow. Depending on the level of magnetic field rotation across the depression, solar wind magnetic holes (SWMHs) are typically classified as linear or rotational holes (Turner et al., 1977; Volwerk et al., 2021). These pressure-balanced structures have been observed at various heliocentric distances and plasma environments and can appear in different sizes (Burlaga et al., 1990; Karlsson et al., 2021; Madanian et al., 2020; Sperveslage et al., 2000; Wang et al., 2020). SWMHs can bypass the bow shock almost intact and appear in the magnetosheath plasma as a high momentum plasma parcel (Karlsson et al., 2015, 2016). Generation mechanism of MHs has been a point of debate (Tsurutani et al., 2011). Several studies have determined that linear holes are associated with mirror mode waves in high beta plasmas (Balikhin et al., 2012; Burlaga et al., 2007; Volwerk et al., 2021). However, a consistent process for generation of rotational holes has not been identified.

In this paper we analyze the interaction of an RCS and its associated SWMH with Earth's bow shock and magnetopause using a combination of multi spacecraft observations and a convection model. Given the relatively high occurrence rate of RCSs, it is important to have a better understanding of their impacts on plasma boundaries around Earth. In Section 2, details of observations at several plasma boundaries and environments are shown. Discussions of results are provided in Section 3, and the paper is concluded in Section 4.

2. Observations

We use data from the Advanced Composition Analyzer (ACE; Stone et al., 1998), Wind (Harten & Clark, 1995), Cluster (Escoubet et al., 2001), Time History of Events and Macroscale Interactions during Substorms (THEMIS; Angelopoulos, 2008), and the Magnetospheric Multiscale (MMS; Burch et al., 2016) missions. For the Cluster constellation, plasma data are only available from Cluster4 during the event studied here. Also, Cluster3 and 4 spacecraft travel very similar orbits and make nearly identical measurements. As such, Cluster3 data will not be discussed. Similarly, the four MMS spacecraft are in a close tetrahedron formation (less than 25 km intra-spacecraft separation) during this event. We only use data from satellite 1 (MMS1). The spatial scale of the structure analyzed in this study is much larger than the MMS spacecraft separation, and kinetic-scale differences in observations of different MMS spacecraft are not considered. Positioning of these spacecraft on the dayside provide an opportunity for thorough analysis of the RCS interaction with Earth's bow shock and the magnetopause. All vector quantities in the paper are expressed in the geocentric solar magnetic (GSM) coordinate system in which the x-axis points toward the Sun, the y-axis is perpendicular to Earth's magnetic dipole axis, and z completes the right-hand triple.

2.1. RCS in the Solar Wind

The RCS is initially observed by two solar wind monitors at Lagrange point 1. Figures 1a and 1b show the IMF profile measured by ACE and Wind spacecraft, respectively, for a time interval between 07:50:00 and 09:30:00 UT on 20 November 2018. The ACE spacecraft is at (239.1, −15.9, 26.5) R_E (R_E = Earth radius), while the Wind spacecraft is downstream from ACE at (195.7, −29.2, 7.7) R_E. Comparing the two time series, there are a few magnetic depressions at the beginning of the interval in ACE data which seem to have been replenished during the transport to Wind. We focus on the magnetic hole structure in the middle of the interval in Figure 1a between 08:31:28 and 08:35:24 UT. Throughout this paper, we consider the field rotation/reversal due to the RCS occurring throughout the entire SWMH period as a single structure and refer to it as the "structure" or the RCS. Once the SWMH crosses the bow shock, we refer to the associated magnetic depression in the magnetosheath as MH. The magnetic field depression ratio is defined as $\delta B = |B_{in} - B_{out}|/B_{out}$, where B_{in} and B_{out} are the average field strength inside and outside the SWMH, respectively. ACE measures a δB of 0.50 for this structure. A very similar and comparable depression ratio of 0.69 is seen in Wind data between 08:39:14 and 08:48:25 UT, corresponding to the same structure transported by the solar wind. However, at times the magnetic field strength inside the SWMH drops to lower values in Wind data compared to ACE.

The magnetic field and bulk plasma flow velocity components for the highlighted sub-interval are shown in Figures 1c–1e. The data are from the Wind spacecraft. The vertical dashed lines mark the boundaries of the structure which in different plasma environments is recognized by simultaneous observations of a rotation in the magnetic field, accompanied by a decrease in the magnetic field strength, and an enhancement of the plasma density. The first vertical dashed line is drawn at t_i (the time at the leading edge) selected at the beginning of the field rotation, while the second vertical dashed line is drawn at t_f (the time at the trailing edge) determined when the magnetic field strength returns to values before t_i. In Figure 1 however, different components of the magnetic field approach the post current sheet values at different rates. By 08:47:54 UT, the field strength (dominated by B_y) has mostly reached the IMF strength in the pristine solar wind flow before t_i. But B_z reversal is still occurring. As such, we select t_f a few seconds later at 08:48:25 UT when the field rotation has completed in all three components. Similar conditions exist on the leading edge of the structure in observations near the bow shock and inside the magnetosheath. For these cases, we identify t_i when the clock angle reaches its minimum value inside the MH.

The magnetic field rotation is evident in the cone ($\arcsin(B_x/|B|)$) and clock ($\arctan(B_z, B_y)$) angles in Figure 1f. A cone angle of 0° indicates an IMF vector in the plane perpendicular to the Sun-Earth line. In that plane, the clock angle is measured from the $+y$-axis and varies in the $0 - 2\pi$ range. Before the crossing of the current sheet, the IMF has a cone angle −42° and a clock angle of 289°. Immediately after the field rotation at 08:39:12 UT, the cone and clock angles change to 35° and 126°, respectively. At the trailing edge, the cone angle approaches 20° and the clock angle reaches 176°. The magnetic shear angle (α) across the structure is 119.6° at ACE and reduces to 118° at Wind.

The structure also appears to be bifurcated, as commonly observed in solar wind RCSs (Mistry et al., 2015), with field components plateaued near its center. We also observe both correlated and anti-correlated changes in **V** and

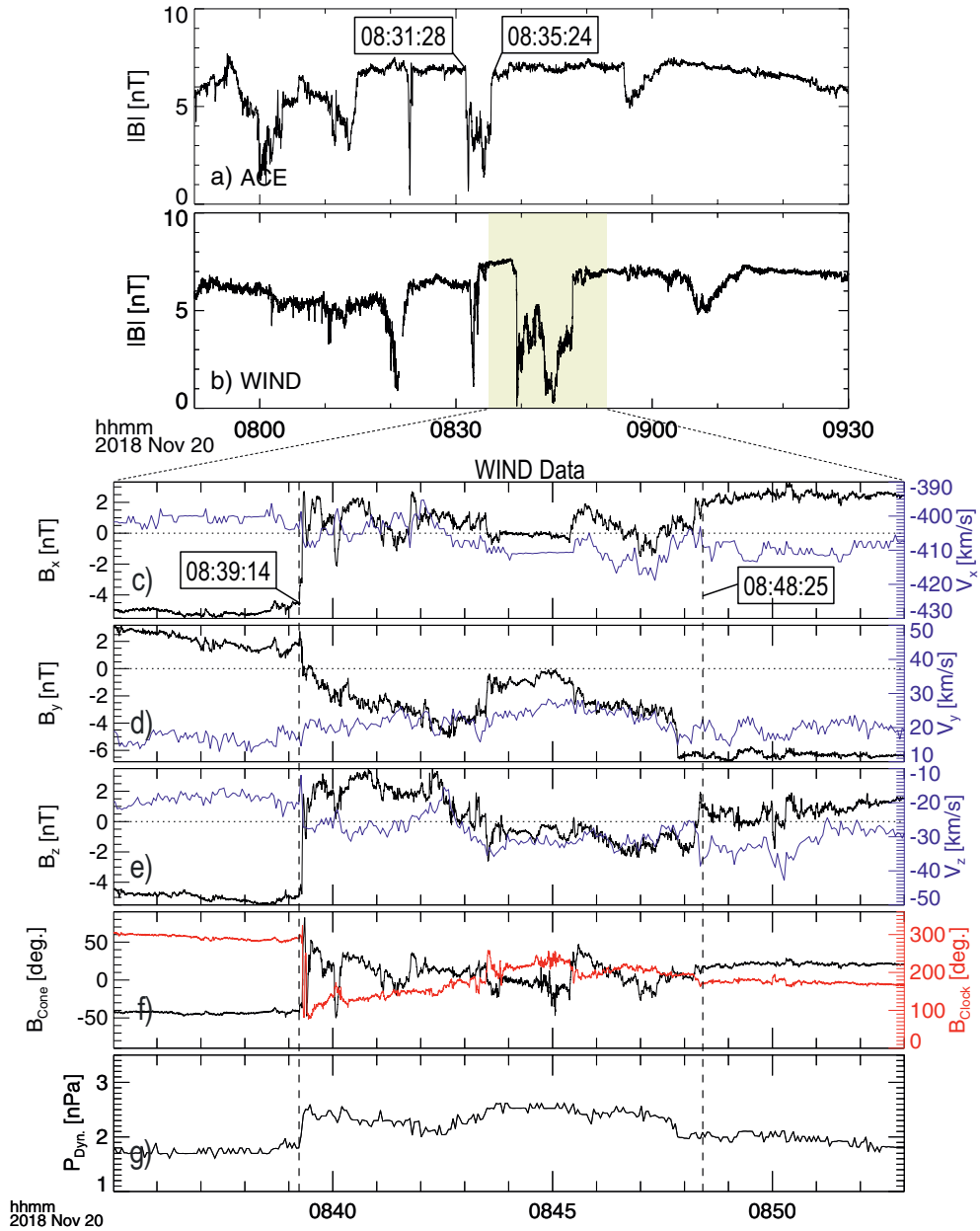

Figure 1. Solar wind magnetic field, flow velocity, and dynamic pressure for an RCS on November 20, 2018. Panels (a) and (b) show the IMF strength measured by ACE and Wind spacecraft, respectively. Panels (c–e) show GSM components of the magnetic field in black and the flow velocity in blue measured by Wind for the highlighted interval in (b). Panel (f) shows the magnetic field clock angle in red and the cone angle in black, and the dynamic pressure is shown in (g). The RCS and its SWMH boundaries (t_i and t_f) are marked with time tags in ACE data in panel (a), and with vertical dashed lines in Wind data in panels (c–g).

B, which are best seen along the y component in Figure 1d. Subtle changes in the flow velocity (~15 km/s from the background solar wind) are most likely due to the reconnection exhaust. There are also velocity variations in the x and z components. The local Alfvén speed ($v_A = |\mathbf{B}|/\sqrt{\mu_0 \rho}$ where ρ is the plasma mass density and μ_0 is the vacuum permeability) on average is relatively low (~22 km/s) throughout the period which limits the outflow speed of exhaust jets. Figure 1g shows an increase in the solar wind dynamic pressure between the vertical dashed lines. The dynamic pressure is in principle a tensor that relates the pressure tensor in the plasma rest frame to that measured in another frame moving with the bulk plasma flow speed. In the solar wind, the tensor element associated with the radial flow component dominates all other values in the tensor and the dynamic pressure is

Table 1
Properties of the SWMH Observed by Different Spacecraft

Region	Source	α (°)	δB	n[a] (cm^{-3})	δt (s)	t_i	t_f	β[a]	$V_{Alf.}$[a] (km/s)	r_{GSM} (R_E)
SW	ACE[b]	119.6	0.5	5.4(–)	236	8:31:28	8:35:24	5.2(0.48)	32.8(67.4)	(239.7, −15.9, 26.5)
	WIND	118.2	0.69	8.7(6.6)	551	8:39:14	8:48:25	22(1)	22.6(64.9)	(195.7, −29.9, 7.6)
BSh	MMS	122.3	0.49	11.5(9.8)	302	9:32:42	9:37:44	20.6(4.2)	23(47.1)	(3.9, 21.1, −2.8)
	THD[c]		0.67	–	274	9:33:07	9:37:42	–	–	(11.8, −3.4. 5.9)
	THE[c]		0.67	–	272	9:33:23	9:37:55	–	–	(11.1, −5.1, 6.3)
MSh	THA	103.2	0.7	37.4(27.5)	335	9:35:27	9:41:03	47.1(2.8)	38.8(125.3)	(9.0, −3.7, 5.8)
MP	C1[d]	–	–	–	30	9:39:16	9:39:46	–	–	(0, 14.5, 2.4)

Note. SW: Solar wind, BSh: Bow shock, MSh: Magnetosheath, MP: Magnetopause.
[a]Values in () are measured outside the magnetic hole. [b]Low time resolution plasma measurements. [c]Plasma data contaminated by foreshock ions. [d]Plasma data unavailable, partial encounters.

determined from $P_{dyn.} = \rho v^2$, where v is the flow speed. Inside the SWMH, the plasma density increases from 6.4 to 8.5 cm^{-3} and the plasma temperature rises from 7.7 to 12.4 eV. These observations are consistent with an extended RCS in the solar wind (Gosling et al., 2005). At the same time, these variations are unlikely to be associated with heliospheric current sheet (HCS) crossings, as characteristic changes in pitch angle distribution of strahl electrons intrinsic to HCS crossings are not observed (Kahler et al., 1998; Kahler & Lin, 1994).

The event duration increases from 236 s at ACE to 551 s at Wind. This expansion suggests that either dynamic plasma processes within the structure have caused expansion of the current sheet thickness, or different spacecraft are at different distances to the X-line of an expanding exhaust. Nevertheless, the RCS and its SWMH are a magnetohydrodynamic (MHD) scale structure. The normal vector to the RCS plane obtained from the minimum variance analysis (MVA) of the Wind magnetic field data is $n_{cs} = (-0.84, -0.26, 0.45)$. The normal vector at ACE deviates from this vector by less than 8°. This difference could be due to rotation of the plane phase, or uncertainties associated with applying the MVA. Nonetheless, the large ratio of intermediate to minimum eigenvalues of the variation matrix (see the Supporting Information section), and small field variations along the minimum variance direction suggest that the MVA results are reliable and the normal vector is determined reasonably well. Figure S1 in Supporting Information S1 shows more details of our MVA analysis.

ACE and Wind spacecraft are ∼50 R_E apart during this event, mostly along the Sun-Earth line. Spacecraft positions are listed in Table 1. Based on the solar wind bulk flow velocity and the RCS normal vector, the expected travel time between the two spacecraft is 420 s, that is within 10% of the time lag (466 s) of observing the leading edge of the RCS (see Table 1). Distinct change in the clock angle accompanied by reduced magnetic field strength and increased plasma density and dynamic pressure are features that enable distinguishing and tracking the structure through different plasma environments and spacecraft data sets, although the absolute value of each parameter significantly varies in different environments. In addition, the solar wind plasma remains calm and steady for more than 5 minutes on either side of the structure which reduces the amount of turbulence and interference at the bow shock and in the magnetosheath and simplifies the interpretation of time series data.

2.2. Arrival at the Bow Shock

At around 09:32:00 UT (corresponding to a ∼53 min transition time to the nose of the bow shock from L1), several Earth-orbiting spacecraft are spread across the dayside bow shock, magnetosheath, and magnetopause. Figure 2 shows trajectories of THEMIS, Cluster, and MMS spacecraft projected on the xy (left) and xz (right) planes of the GSM coordinates for a three-hour interval starting at 09:30:00 UT. Before the SWMH arrives at the bow shock, the MMS spacecraft are on an inbound trajectory inside the magnetosheath. THD (THEMIS-D) and THE spacecraft are in the solar wind and near the nose of the bow shock, while THA is inside the magnetosheath and closer to the magnetopause boundary. Cluster1, 2, and 4 spacecraft are inside the magnetosphere boundary layer, with Cluster1 being closest to the boundary at the dusk flank side. In Figure 2, we also show modeled magnetopause (solid lines) and bow shock (dashed lines) boundaries for two sets of upstream conditions. The model parameters including $P_{dyn.}$, the Alfvénic Mach number ($M_{Alf.} = v_{sw}/v_A$, where v_{sw} is the solar wind flow

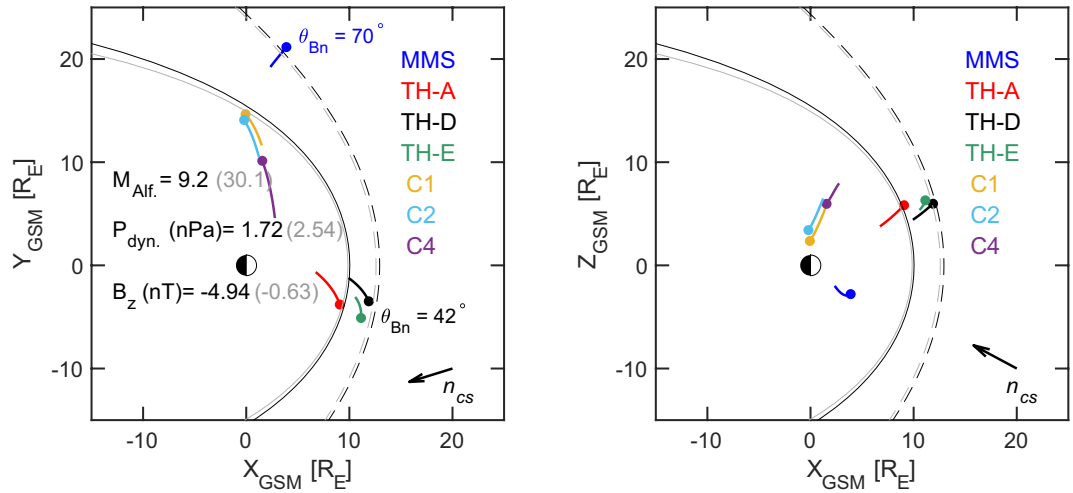

Figure 2. Spacecraft positions projected on the *xy* (left) and *xz* (right) planes of GSM coordinates. The MMS1 spacecraft (MMS) is shown in blue, THA in red, THD in black, THE in green, Cluster1 (C1) in yellow, Cluster2 (C2) in cyan, and Cluster4 (C4) in purple. Trajectories are shown for a 3-h interval between 09:30:00 and 12:30:00 UT on 20 November 2018. Filled circles mark the beginning of the interval. The dashed parabolas represent the bow shock boundary modeled after Farris and Russell (1994), while the solid parabolas are the modeled magnetopause boundary (Shue et al., 1998). The gray boundaries are model predictions under upstream conditions inside the magnetic depression of the RCS. The model parameters are annotated on the left panel. The normal vector to the RCS plane (n_{cs}) is marked on the lower right corner of each panel. The shock angles (θ_{Bn}) correspond to the IMF orientation before the event onset at MMS1 and THD.

speed along the normal vector at the nose of the bow shock) and the B_z component of the IMF are annotated on the left panel. The gray lines show the standoff distance of boundaries for conditions inside the SWMH (gray parameters). To have a better contrast, the parameters inside the SWMH are selected around the lowest magnetic field strength. The modeled bow shock and magnetopause boundaries in Figure 2 are drawn at the zero plane of the third coordinate. The predicted boundaries are based on statistical models fitted on many bow shock crossings and assume cylindrical symmetry around the aberrated Sun-Earth line. These factors can cause discrepancies between the predicted plasma environment in which each spacecraft resides and in-situ observations.

Figure 3 shows an overview of in-situ measured plasma and field data from MMS1. The magnetic field data are provided by the magnetometer system (Russell et al., 2016) and plasma particles are probed by the Fast Plasma Investigation (FPI) instrument (Pollock et al., 2016). The spacecraft is initially in the magnetosheath but it emerges out to the solar wind as the RCS hits the bow shock. The magnetic field rotation associated with the onset of the RCS is observed by MMS1 inside the magnetosheath at 09:32:42 UT. The rotation is accompanied by a decrease in the magnetic field strength corresponding to the shocked SWMH plasma. MMS1 remains inside the magnetosheath for another 119 s before the bow shock layer moves inward past the spacecraft position. At the leading edge of the RCS, the magnetic field clock angle changes from 275° to ∼160° and in general, both cone and clock angles show similar patterns to those observed in the solar wind, although magnetic field fluctuations are significantly higher in the magnetosheath.

The electron energy spectrogram in Figure 3c shows that the energy flux of accelerated solar wind electrons increases when the SWMH crosses the bow shock, as compared to the distributions in the magnetosheath plasma and before the event onset. As the bow shock recedes, MMS1 crosses a shock layer formed against the SWMH. Inside the SWMH, the shock obliquity decreases but it remains in the quasi-perpendicular regime ($\theta_{Bn} \sim 56°$). The low magnetic energy density and increased plasma density within the hole result in a high plasma β (the ratio of the plasma thermal pressure to magnetic pressure) and low v_A upstream of the shock (see Table 1). Precursor whistler waves are suppressed upstream of the shock (Fairfield, 1974). Instead, we observe high amplitude quasi-periodic magnetic pulsations with a period of 2 s in the spacecraft frame. These waves can play a role in enhancing the population of accelerated electrons. The bulk plasma velocity components in Figure 3d indicate that the solar wind slowdown along the *x*-axis and deflection along the *y*-axis are dominant downstream of the bow shock and the reconnection exhausts are obscured in the sheath plasma. There are however, slight differences in the flow velocity in the magnetosheath between the onset of the field rotation and the bow shock crossing at

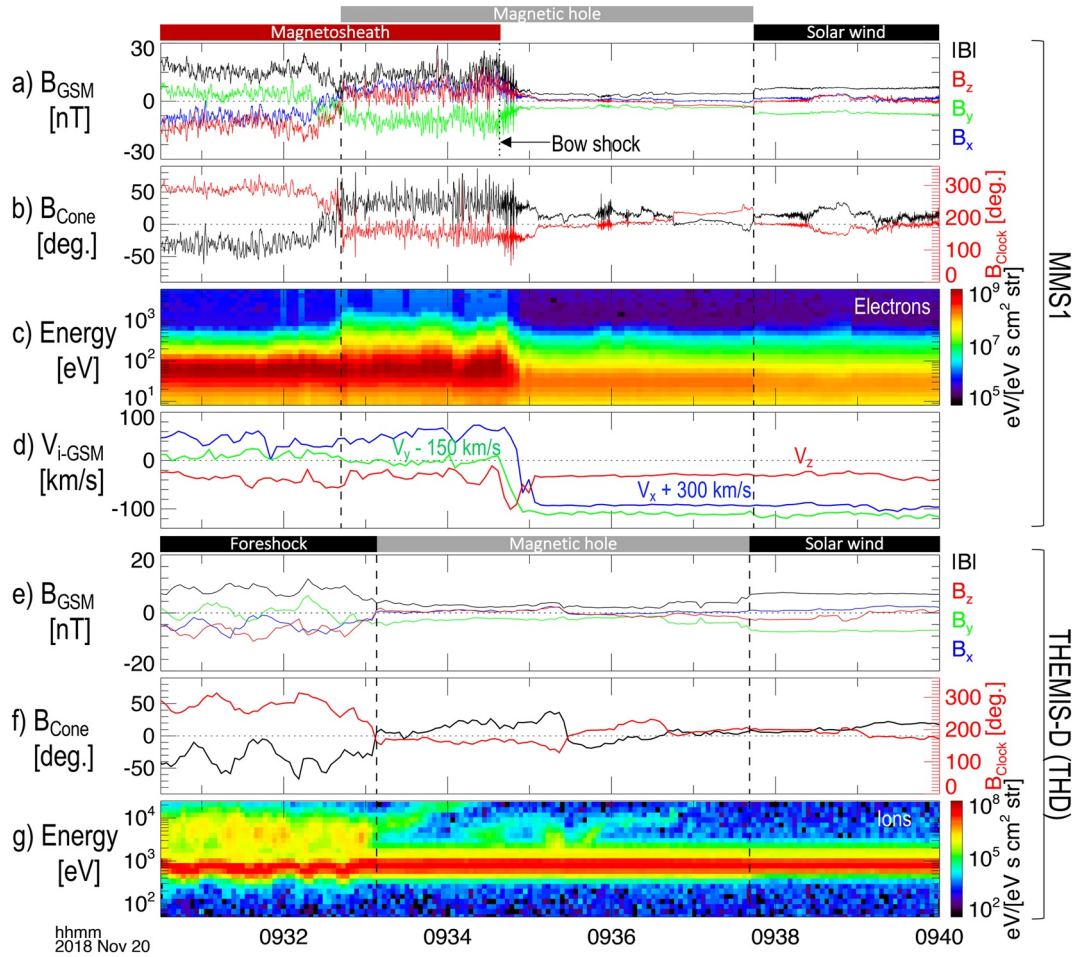

Figure 3. MMS1 and THD observations of the RCS and the SWMH crossing the bow shock. The MMS1 spacecraft is initially in the magnetosheath near the dusk side flank region. Panels (a–d) show MMS1 measurements of the magnetic field components and magnitude, magnetic field cone and clock angles, electron energy spectrogram, and components of the ion bulk flow velocity, respectively. The V_x and V_y velocity components in panel (d) are shifted by +300 and −150 km/s, respectively. Panels (e) and (f) show the magnetic field, and cone and clock angle data from THD spacecraft positioned closer the nose of the bow shock. The vertical dashed lines mark the boundaries of the SWMH as observed by MMS1 and THD. The vertical dotted line on panel (a) marks the bow shock crossing at 09:34:38 UT.

09:34:38 UT (the dotted line in Figure 3a). For instance, V_y decreases by ∼17 km/s from 160 to 143 km/s. Similar variations also exist in V_z. These small changes are superimposed on the flow deflection and slowdown incurred at the bow shock, though they are comparable in strength to changes due to reconnection exhausts within the RCS (Figures 1c–1e).

THD observations of the RCS and SWMH are shown in Figures 3e–3g. During this time, THD is in the foreshock region upstream of the quasi-parallel side of the shock. THD magnetic field data are from the flux gate magnetometers (Auster et al., 2008), and plasma data are from the electrostatic analyzers (McFadden et al., 2008), and the solid state telescopes. Before the field rotation, THD measures high levels of turbulence (Figure 3e) associated with a significant flux of suprathermal foreshock ions in this region. These ions, visible in the ion energy spectrogram in Figure 3g at energies above the solar wind beam energy at ∼900 eV, can create plasma waves through a variety of instabilities (Scholer & Burgess, 1992). Rotation of the field at ∼09:33:08 UT results in a traveling foreshock (Kajdič et al., 2017), and disappearance of waves. The shock angle inside the SWMH and immediately after the field rotation is about 72° and it mostly remains above 45° throughout the SWMH passage. The clock angle changes from ∼280°–168°, while the cone angle changes from −32° to ∼12°. The THE spacecraft is about 0.7 R_E downstream from THD and very close to the bow shock but still in the foreshock region. THE observations (not shown) revealed similar RCS features to those in THD data, except that foreshock turbulence at THE is much

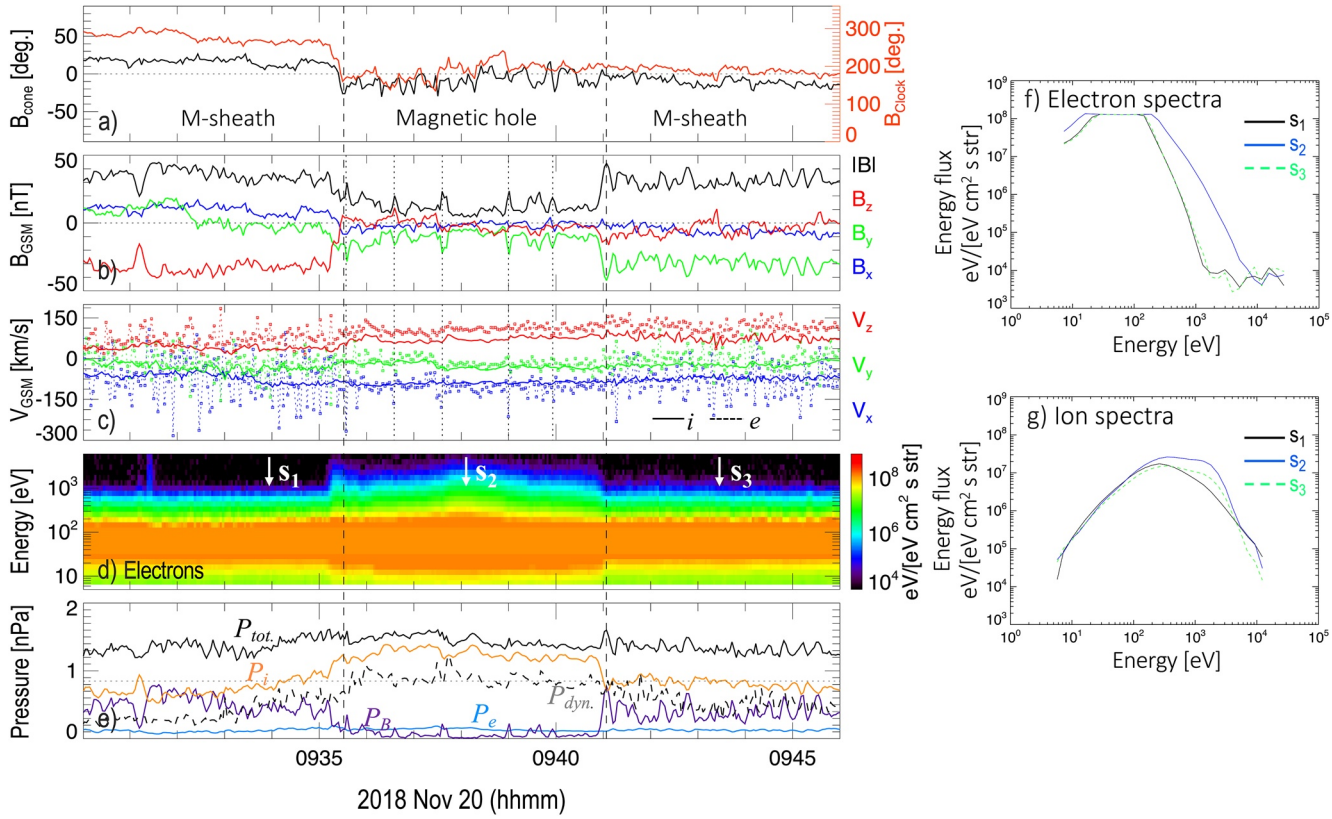

Figure 4. Observations of the RCS in the magnetosheath by THA. Panels show: (a) the cone and clock angles, and annotated magnetosheath (M-sheath) and magnetic hole intervals, (b) magnetic field components and strength, (c) ion (solid lines) and electron (dotted lines) velocity components, (d) electron energy spectrogram, (e) pressure terms including the electron thermal pressure (P_e, blue), ion thermal pressure (P_i, red), magnetic pressure (P_B, purple), dynamic pressure ($P_{dyn.}$, gray-dotted), and the total pressure ($P_{tot.}$, black). The horizontal dashed line in panel (e) is drawn at half the pristine solar wind dynamic pressure (0.86 nPa). The two vertical dashed lines on these panels mark the magnetic hole boundaries, while vertical dotted lines in panels (b–c) correspond to a select number of magnetic peaks inside the hole to emphasize their association with electron jets. Panels (f) and (g) show, respectively, electron and ion energy spectra at three timestamps identified on panel (d).

more intense with sporadic high amplitude steepened waves. The density of backstreaming ions is also higher at THE. The RCS is observed by THE 16 s after THD (as indicated by t_i times in Table 1) corresponding to an average radial solar wind flow speed of 292.8 km/s. This solar wind slowdown is due to foreshock effects that begin much farther upstream of the shock and beyond the THD position, as backstreaming ions can travel long distances upstream of the shock along the magnetic field lines (Eastwood et al., 2005).

2.3. Changes in the Magnetosheath and at the Magnetopause

SWMHs can bypass the bow shock and travel through the magnetosheath in the form of diamagnetic plasmoids (Karlsson et al., 2015). In Figure 3 we showed that the characteristic field rotation across the RCS in the solar wind can be clearly identified in magnetosheath plasma immediately downstream of the quasi-perpendicular bow shock in MMS1 data. During this event, THA is at (9.0, −3.7, 5.8) R_E in the magnetosheath and downstream of the quasi-parallel side of the bow shock (see the shock angle map in Figure S2 in the Supporting Information section). Figure 4a shows magnetic field cone and clock angles measured by THA, while the magnetic field components and strength are shown in Figure 4b. Before the structure arrives at THA, the B_x component of the magnetic field in the sheath plasma is pointing sunward, resulting in a positive cone angle of 14.5°. This B_x reversal at THA is due to draping of the sheath plasma (Coleman, 2005; Spreiter et al., 1966). The clock angle at the leading edge of the structure changes from 264° to 166° similar to changes observed at THD and MMS1. Foreshock effects cause noticeable slowdown of the solar wind on the leading edge of the MH compared to the trailing edge, and the structure's trailing edge is processed faster through the shock than its leading edge. δB at THA is about 0.70, although at times the magnetic field strength reduces to half of the pristine IMF strength. The level

of plasma turbulence inside the magnetic hole also decreases significantly compared to the surrounding magnetosheath plasma. Several sporadic magnetic peaks are observed inside the MH that are linearly polarized and are accompanied by earthward directed transverse electron jets. Ions do not seem to be affected, which indicates that peaks are on electron kinetic scales. The magnetic peaks also seem to be unrelated to mirror mode waves as they lack any electron density enhancements. These peaks tend to propagate in the background ion plasma rest frame, though their generation mechanism remains unexplained (Yao et al., 2017).

In Figure 4e we show the plasma pressure terms including the ion (electron) thermal pressure $P_{i(e)} = n_{i(e)}k_b T_{i(e)}$, where $n_{i(e)}$ and $T_{i(e)}$ are the density and average temperature of ions (electrons), and k_b is the Boltzmann constant. The magnetic pressure $P_B = |B|^2/2\mu_0$ and the total pressure $P_{tot.} = P_i + P_e + P_B$ are also shown. The decrease in the magnetic pressure is compensated by the increase in ion thermal pressure, so the structure remains roughly pressure balanced as it travels through the magnetosheath. The flow dynamic pressure $P_{dyn.}$ is also shown on this panel to emphasize that although there are no high-speed (ion) plasma jets, the dynamic pressure within the MH is significantly higher than the surrounding magnetosheath plasma, and at times even higher than half the solar wind dynamic pressure (horizontal dotted line), which is a threshold used in some studies to identify magnetosheath jets (Escoubet et al., 2020). Variations in $P_{dyn.}$ are driven by n_i which is affected by the propagation pattern of the RCS in the magnetosheath.

Figures 4f and 4g show electron and ion energy spectra measured at three timestamps before, within, and after the MH. Inside the MH, electron and ion energy distributions broadens, with a higher flux of accelerated particles in the few keV range. Accelerated electrons remain restricted to the MH boundaries showing more abundance near the center. They are likely remnants of heating and acceleration processes at the bow shock rather than being generated at a nearby magnetopause reconnection zone. Although THA is close to the magnetopause boundary, there are no ion jets in the data to indicate proximity to a reconnection zone. The electron temperature inside the magnetic hole is isotropic, and the average electron temperature slightly reduces from the ambient magnetosheath plasma. The ion temperature is anisotropic, with higher temperatures perpendicular to the field. The density and the average temperature of ions increase inside the MH. Changes in particle energy distributions have implications for energy input at the magnetopause which we discuss in Section 3.3.

Variations in the plasma dynamic pressure can have an influence on the shape of the magnetopause and its standoff distance. The upstream IMF variations can also dramatically change the magnetic field topology and reconnection zones at the magnetopause (Trattner et al., 2016, 2020). We use a model to estimate the probable magnetic field topology at the magnetopause and calculate the maximum magnetic shear angle between the convected IMF and the geomagnetic field (Trattner et al., 2007). The model takes into account convection of the solar wind through the magnetosheath, geomagnetic field at the magnetopause, and draping effects, to predict regions across the magnetopause prone to reconnection. In Figure 5a we show the maximum shear angle map at the magnetopause for solar wind conditions before the onset of the RCS when the IMF is southward. High magnetic shear angles (red colors) are formed along the y-axis and mostly above the magnetic equatorial plane. The white streaks are regions with almost exactly anti-parallel field configuration. The map in Figure 5b is generated based on plasma conditions within the SWMH, where the dynamic pressure has increased and B_z is very small. The white line connecting the two loci is the predicted component reconnection line that extends more than 15 R_E across the magnetopause. Under SWMH plasma conditions, model predictions suggest that Cluster1 and 2 spacecraft are farther from active reconnection zones and are outside the magnetopause boundary.

Indeed all Cluster spacecraft are initially inside the boundary layer, consistent with model predictions. Cluster1 and 2 are near the flank region of the magnetopause on the dusk side and downstream of the quasi-perpendicular side of the bow shock, while Cluster4 is deeper inside the magnetosphere and farther away from the magnetopause boundary. Magnetic field measurements from Cluster1, 2, and 4 (Balogh et al., 2001) are shown in Figure 6. All three spacecraft observe perturbations in the geomagnetic field between 09:36:30 and 09:41:30 UT, corresponding to the time when the solar wind RCS entered the magnetosheath. Magnetic perturbations decrease with spacecraft distance to the magnetopause. Cluster1 is closest to the magnetopause boundary and records the highest level of magnetic fluctuations that include B_z field reversals. The only source of $-B_z$ at the position of Cluster1 inside the boundary layer is from the magnetosheath plasma and specifically from the period before the onset of the RCS. After crossing the bow shock and traveling through the magnetosheath, the RCS impacts the magnetopause and causes an inward motion of the boundary near Cluster1. The gradual boundary crossing on one side is followed by a fast rebound on the other side as evident in B_z variations. The Cluster2 spacecraft is

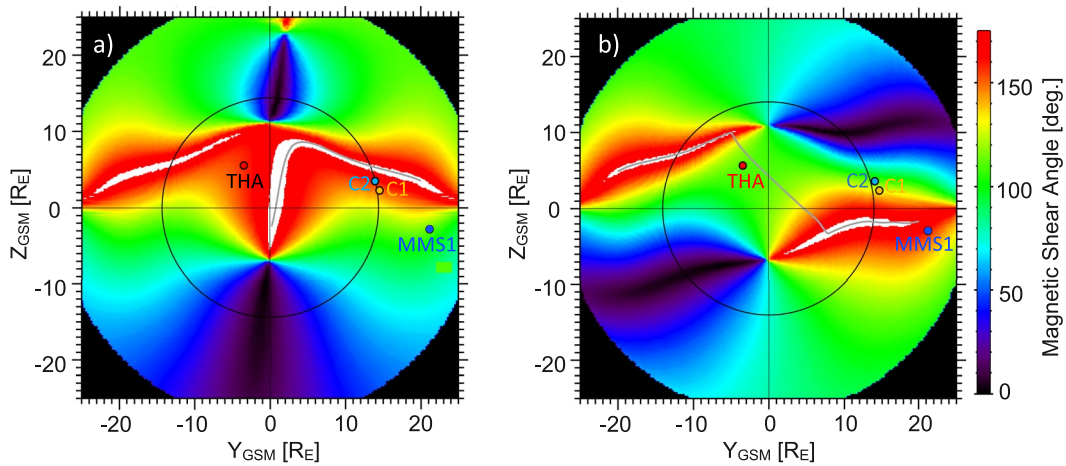

Figure 5. Maps of the magnetic shear angle between the convected IMF and the dipole field, and possible reconnection zones at the magnetopause. Each map shows a cross-sectional view of the magnetopause (black circle) viewed from the Sun. (a) The shear angle map at the magnetopause under convected solar wind conditions before the RCS onset (i.e., $-B_z$), (b) shear angles based on the solar wind conditions inside the magnetic hole. The white streaks are regions with almost exactly anti-parallel field configuration (within 3°). The positions of THA, MMS1, Cluster1, Cluster2 spacecraft are identified for reference.

~0.4 R_E apart from Cluster1 along the local normal direction to the magnetopause, but it does not see the motion of the boundary.

3. Discussion

Based on correlated and anti-correlated variations in B_y and V_y, enhancements in plasma density and temperature, and the high magnetic shear angle we classify the magnetic depression event between 08:39:14 and 08:48:25 UT in Wind data as an RCS. We track the structure in other plasma environments by observing the distinct change in the magnetic field clock angle, followed by a depression in the magnetic field strength, and an increase in plasma density. These characteristics are consistently observed in different data sets and plasma environments but with varying values and ranges (see Table 1). We determine the structure's orientation in the solar wind and show how it impacts the bow shock and magnetopause using observations from multiple Earth orbiting spacecraft. The

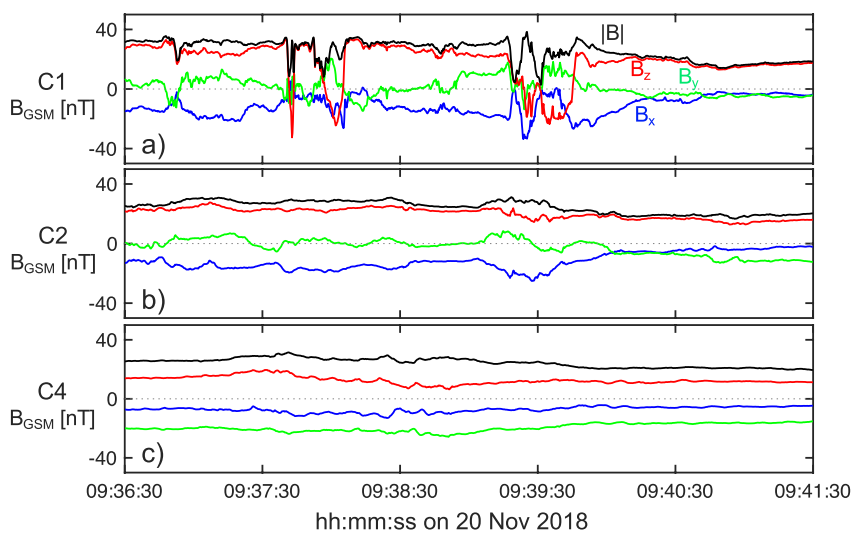

Figure 6. Three Cluster spacecraft observations of the event inside the magnetosphere boundary layer. Panels (a–c) show the magnetic field data from Cluster1, 2, and 4, respectively.

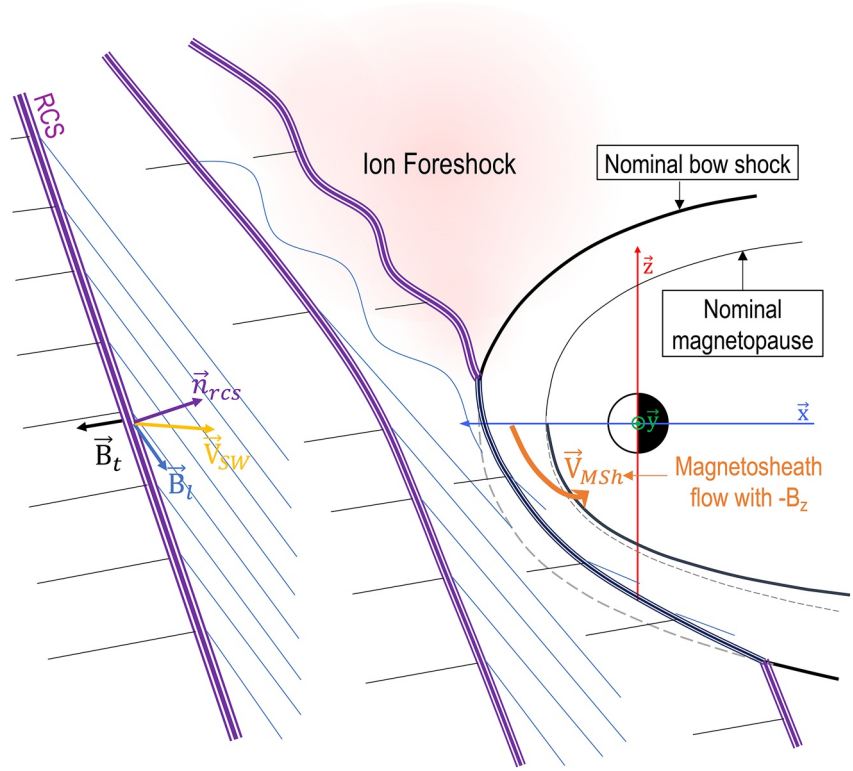

Figure 7. A schematic illustration of the RCS and the SWMH (purple line) interacting with the bow shock and the magnetopause. The magnetic field lines on the leading edge $(\vec{\mathbf{B}}_l)$ are indicated with blue lines. The magnetic field lines on the trailing edge $(\vec{\mathbf{B}}_t)$ are shown in black. The solar wind flow vector $(\vec{\mathbf{V}}_{SW})$ and the normal vector the RCS plane $(\vec{\mathbf{n}}_{rcs})$ are also shown. The magnetosheath plasma flow carrying $-B_z$ field downstream of the bow shock is indicated with $\vec{\mathbf{V}}_{MSh}$. The dashed line segments indicate the nominal position of the boundaries before the start of the interaction with the RCS.

normal vector to the RCS plane at ACE is about 8° different than that at Wind. The event duration also increases from ACE to Wind, and then decreases at MMS1 near the bow shock. These differences can be due to the rotation of the RCS plane during the transit from L1 to Earth's bow shock. Ongoing reconnection and plasma instabilities can also modify the current sheet structure.

3.1. Asymmetric Interaction and Global Impact

THD and MMS1 spacecraft are separated by more than 27 R_E across the bow shock, while THA and Cluster1 are ~20 R_E apart across the magnetopause boundary. We show that, with certain time lags, all spacecraft measured signatures of the same structure which suggests that the solar wind RCS plane covers most of the dayside bow shock surface. Even though MMS1 is 7.2 R_E downstream of THD and in the magnetosheath, it observes the structure 24 s before THD, indicating that the RCS with high momentum plasma enters the magnetosheath through the flank region of the bow shock first and then through the subsolar region. This order of observations also agrees with our estimate of the RCS plane orientation which hits the $(+x, +y, -z)$ quadrant of the bow shock first. Furthermore, before the SWMH arrival, THD is upstream of the quasi-parallel side of the shock, where foreshock effects tend to significantly decelerate the solar wind. Backstreaming foreshock ions travel far distances upstream of the shock along the magnetic field line and perturb the solar wind. As such, the upstream structure arrives at and crosses the quasi-perpendicular side of the bow shock before the quasi-parallel side (Turc et al., 2020). This asymmetric interaction across the bow shock will inevitably transfer downstream and create asymmetric interaction zones at the magnetopause boundary (Keika et al., 2009; Webster et al., 2021).

The schematic in Figure 7 shows a summary of our observations, illustrating the dynamics of the RCS interaction at different stages and environments. The schematic shows that parts of the bow shock and magnetopause are displaced and pushed inward after interacting with the RCS. THA and MMS1 observations of magnetosheath

plasma indicate that inside the MH, B_z is essentially zero or even slightly positive. However, because of the misalignment of the RCS plane normal vector with the solar wind velocity vector and asymmetric effects discussed earlier, when parts of the magnetopause are pushed inward, Cluster1 observes magnetosheath flow with $-B_z$ field originated from upstream regions near the subsolar point where the RCS has not reached yet ($\vec{\mathbf{V}}_{MSh}$ in Figure 7). Since the bow shock and the magnetopause are essentially local pressure-balanced boundaries between two plasma environments, the asymmetric interaction of the RCS results in deformed boundaries. As the schematic in Figure 7 shows, the bow shock (and the magnetopause) adjusts itself in response to a change in the direction of the highest dynamic pressure, which in this case is caused by the increase in plasma density within the RCS and its propagation direction is aligned with the RCS plane orientation.

3.2. Energy Input and Reconnection at the Magnetopause

Ion and electron velocities in Figure 4c show that THA observes a draped plasma flow pointed mostly Earth-ward and northward, which is consistent with the position of THA in the magnetosheath. At the leading edge of the magnetic hole, field rotation is accompanied by an increase in V_z, suggesting that flow deflection increases as the structure propagates through the magnetosheath. This flow pattern is consistent with the asymmetric encounter of the solar wind RCS plane with the bow shock, which can preferentially drive the magnetosheath plasma along its normal vector.

The electron and ion energy spectra lines in Figures 4f and 4g show clear enhancements in the flux of accelerated electrons and ions inside the MH. Once these particles reach the magnetopause, they can travel along the geomagnetic field lines and precipitate into the ionosphere through cusp regions. Accelerated electrons are also present in Figure 3c in the portion of the MH that has crossed the bow shock, indicating that acceleration of electrons to high energies is associated with RCS and SWMH interactions at the bow shock. Low v_A and high plasma β within the SWMH and upstream of the bow shock also have implications for generation of upstream instabilities (Gary, 1993; Madanian et al., 2021; Petrukovich & Chugunova, 2021). When magnetosheath is dominated by the MH plasma, coupling of the solar wind to the magnetosphere shifts to the low-latitude boundary layer (closed field lines), and through hydrodynamic forcing (Maynard et al., 2011). Large-scale RCS and SWMH events change the rate of energy input into the ionosphere-magnetosphere system either by introducing precipitating accelerated particles or by modulating the ion transport at ionospheric altitudes near the polar cap regions. More observational and simulation studies are required in the future to characterize their effects in those plasma environments. We should also note that THA moment data in Figure 4 are calculated onboard the spacecraft with measurements performed in the reduced mode (i.e., reduced energy and spatial resolutions). The high time resolution of data in this mode however, enables studying physical processes on time scales relevant to the RCS duration. There may be minor calibration issues in data, for instance the difference between the electron and ion V_z velocity component, or electron flux saturation at high count rates which relates to the instrument sensitivity in this mode. Our results and interpretations are not affected by these issues.

Crossing the bow shock can also modify the exhaust flows within the RCS, which can disrupt any ongoing reconnection process (Phan et al., 2011). Survival of the reconnection jets across the bow shock is dependent upon the direction of reconnection exhausts and the bow shock geometry at the point of crossing, which can further contribute to creating variable plasma environments downstream of the bow shock. When the solar wind IMF has already been depleted, for instance through reconnection within the solar wind, the dynamics of reconnection at the magnetopause can become more complicated. Rotation of the magnetic field across the event studied in this paper reduces regions of high magnetic shear angles across the magnetopause (Figure 5b). In addition, the plasma β inside the MH is higher than the surrounding magnetosheath plasma, and much higher than the low-density plasma in the boundary layer. These conditions seem to have adverse effects on the reconnection rate at the magnetopause.

4. Conclusion

In this study, we follow an RCS initially observed in the pristine solar wind upstream of Earth across the bow shock, and through the magnetosheath to the magnetopause. Reconnection in the solar wind converts the IMF energy into plasma kinetic energy, thus depleting the magnetic field strength within the current sheet, while increasing the plasma density and temperature and creating a high momentum plasma layer. Rotational SWMHs

associated with RCS are caused by magnetic reconnection and show noticeable enhancement in both plasma density and temperature. Once reconnection begins in the solar wind flow, there is abundant magnetic energy in the IMF available to the process, and therefore the amount of density buildup and the spatial scale of the magnetic depression can be significant. We show that the RCS enters the bow shock through the flank regions rather than the subsolar point. Upon crossing the bow shock, acceleration of solar wind electrons is more efficient within the magnetically depleted layer, and accelerated electrons remain restricted to the MH inside the magnetosheath (Figure 4d). Determining the nature of the acceleration mechanism at the bow shock and its relation to high amplitude waves are left for our future studies.

The RCS and its SWMH form a high dynamic pressure plasma layer inside the magnetosheath. Given the global nature of the interaction, it would be a misnomer to categorize such a structure as a plasma jet, although it may very well fit the selection criteria of high speed jets (i.e., enhanced dynamic pressure above half the solar dynamic pressure). Nonetheless, similar to high-speed jets, RCS and their SWMHs can cause asymmetric deformation of the magnetopause boundary, and modulate the reconnection rate. Furthermore, the amplitude of magnetic perturbations due to the RCS decreases with distance from the magnetosphere boundary layer (Figure 6), and Earth's magnetosphere seems to act as a "cushion" against the upstream high momentum plasma anomaly. Effects of the RCS and SWMH structures on planets without an intrinsic magnetosphere merit further investigations in the future.

Data Availability Statement

All data used in this study are publicly accessible through https://spdf.gsfc.nasa.gov/pub/data/.

Acknowledgments
We thank the mission operation and instrument teams on ACE, Wind, THEMIS, Cluster, and MMS missions for making their science data available. This work was partially supported by National Aeronautics and Space Administration (NASA) grants NNG04EB99C and 80NSSC21K1461. KJT efforts were supported in part by NASA Grant 80NSSC20K0688. HM thanks support from an ISSI team on magnetic holes.

References

Andreeova, K., Pulkkinen, T. I., Palmroth, M., & McPherron, R. (2011). Geoefficiency of solar wind discontinuities. *Journal of Atmospheric and Solar-Terrestrial Physics*, *73*(1), 112–122. https://doi.org/10.1016/j.jastp.2010.03.006

Angelopoulos, V. (2008). The THEMIS mission. *Space Science Reviews*, *141*(1–4), 5–34. https://doi.org/10.1007/s11214-008-9336-1

Archer, M. O., Horbury, T. S., & Eastwood, J. P. (2012). Magnetosheath pressure pulses: Generation downstream of the bow shock from solar wind discontinuities. *Journal of Geophysical Research*, *117*(5). https://doi.org/10.1029/2011JA017468

Auster, H. U., Glassmeier, K. H., Magnes, W., Aydogar, O., Baumjohann, W., Constantinescu, D., et al. (2008). The THEMIS fluxgate magnetometer. *Space Science Reviews*, *141*(1–4), 235–264. https://doi.org/10.1007/s11214-008-9365-9

Balikhin, M. A., Sibeck, D. G., Runov, A., & Walker, S. N. (2012). Magnetic holes in the vicinity of dipolarization fronts: Mirror or tearing structures? *Journal of Geophysical Research*, *117*(8). https://doi.org/10.1029/2012JA017552

Balogh, A., Carr, C. M., Acuña, M. H., Dunlop, M. W., Beek, T. J., Brown, P., et al. (2001). The cluster magnetic field investigation: Overview of in-flight performance and initial results. *Annales Geophysicae*, *19*(10/12), 1207–1217. https://doi.org/10.5194/angeo-19-1207-2001

Blanco-Cano, X., Preisser, L., Kajdič, P., & Rojas-Castillo, D. (2020). Magnetosheath microstructure: Mirror mode waves and jets during southward IP magnetic field. *Journal of Geophysical Research: Space Physics*, *125*(9). https://doi.org/10.1029/2020JA027940

Burch, J. L., Moore, T. E., Torbert, R. B., & Giles, B. L. (2016). Magnetospheric multiscale overview and science objectives. *Space Science Reviews*, *199*(1–4), 5–21. https://doi.org/10.1007/s11214-015-0164-9

Burlaga, L. F., Ness, N. F., & Acuna, M. H. (2007). Linear magnetic holes in a unipolar region of the heliosheath observed by Voyager. *Journal of Geophysical Research*, *112*(7). https://doi.org/10.1029/2007JA012292

Burlaga, L. F., Scudder, J. D., Klein, L. W., & Isenberg, P. A. (1990). Pressure-balanced structures between 1 AU and 24 AU and their implications for solar wind electrons and interstellar pickup ions. *Journal of Geophysical Research*, *95*(A3), 2229. https://doi.org/10.1029/ja095ia03p02229

Cassak, P. A., & Shay, M. A. (2007). Scaling of asymmetric magnetic reconnection: General theory and collisional simulations. *Physics of Plasmas*, *14*(10), 102114. https://doi.org/10.1063/1.2795630

Coleman, I. J. (2005). A multi-spacecraft survey of magnetic field line draping in the dayside magnetosheath. *Annales Geophysicae*, *23*(3), 885–900. https://doi.org/10.5194/angeo-23-885-2005

Drake, J. F., Swisdak, M., Opher, M., & Richardson, J. D. (2017). The formation of magnetic depletions and flux annihilation due to reconnection in the heliosheath. *The Astrophysical Journal*, *837*(2), 159. https://doi.org/10.3847/1538-4357/aa6304

Eastwood, J. P., Lucek, E. A., Mazelle, C., Meziane, K., Narita, Y., Pickett, J., & Treumann, R. A. (2005). The foreshock. *Space Science Reviews*, *118*(1–4), 41–94. https://doi.org/10.1007/s11214-005-3824-3

Escoubet, C. P., Fehringer, M., & Goldstein, M. (2001). The Cluster mission. *Annales Geophysicae*, *19*(10/12), 1197–1200. https://doi.org/10.5194/angeo-19-1197-2001

Escoubet, C. P., Hwang, K. J., Toledo-Redondo, S., Turc, L., Haaland, S. E., Aunai, N., et al. (2020). Cluster and MMS simultaneous observations of magnetosheath high speed jets and their impact on the magnetopause. *Frontiers in Astronomy and Space Sciences*, *6*, 78. https://doi.org/10.3389/fspas.2019.00078

Fairfield, D. H. (1974). Whistler waves observed upstream from collisionless shocks. *Journal of Geophysical Research*, *79*(10), 1368–1378. https://doi.org/10.1029/ja079i010p01368

Farris, M. H., & Russell, C. T. (1994). Determining the standoff distance of the bow shock: Mach number dependence and use of models. *Journal of Geophysical Research*, *99*(A9), 17681. https://doi.org/10.1029/94ja01020

Farrugia, C. J., Erkaev, N. V., Biernat, H. K., & Burlaga, L. F. (1995). Anomalous magnetosheath properties during Earth passage of an interplanetary magnetic cloud. *Journal of Geophysical Research*, *100*(A10), 19245. https://doi.org/10.1029/95ja01080

Gary, S. P. (1993). *Theory of space plasma microinstabilities*. Cambridge: Cambridge University Press. https://doi.org/10.1017/cbo9780511551512

Gosling, J. T. (2012). Magnetic reconnection in the solar wind. *Space Science Reviews*, *172*(1–4), 187–200. https://doi.org/10.1007/s11214-011-9747-2

Gosling, J. T., Skoug, R. M., McComas, D. J., & Smith, C. W. (2005). Direct evidence for magnetic reconnection in the solar wind near 1 AU. *Journal of Geophysical Research*, *110*(A1), A01107. https://doi.org/10.1029/2004JA010809

Gosling, J. T., & Szabo, A. (2008). Bifurcated current sheets produced by magnetic reconnection in the solar wind. *Journal of Geophysical Research*, *113*(10). https://doi.org/10.1029/2008JA013473

Hamrin, M., Gunell, H., Goncharov, O., De Spiegeleer, A., Fuselier, S., Mukherjee, J., et al. (2019). Can reconnection be triggered as a solar wind directional discontinuity crosses the bow shock? A case of asymmetric reconnection. *Journal of Geophysical Research: Space Physics*, *124*(11), 8507–8523. https://doi.org/10.1029/2019JA027006

Harten, R., & Clark, K. (1995). The design features of the GGS wind and polar spacecraft. *Space Science Reviews*, *71*(1–4), 23–40. https://doi.org/10.1007/BF00751324

Hesse, M., & Cassak, P. A. (2020). Magnetic reconnection in the space sciences: Past, present, and future. *Journal of Geophysical Research: Space Physics*, *125*(2). https://doi.org/10.1029/2018ja025935

Hietala, H., Phan, T. D., Angelopoulos, V., Oieroset, M., Archer, M. O., Karlsson, T., & Plaschke, F. (2018). In situ observations of a magnetosheath high-speed jet triggering magnetopause reconnection. *Geophysical Research Letters*, *45*(4), 1732–1740. https://doi.org/10.1002/2017GL076525

Hietala, H., & Plaschke, F. (2013). On the generation of magnetosheath high-speed jets by bow shock ripples. *Journal of Geophysical Research: Space Physics*, *118*(11), 7237–7245. https://doi.org/10.1002/2013JA019172

Kahler, S., Crooker, N. U., & Gosling, J. T. (1998). Properties of interplanetary magnetic sector boundaries based on electron heat-flux flow directions. *Journal of Geophysical Research*, *103*(A9), 20603–20612. https://doi.org/10.1029/98JA01745

Kahler, S., & Lin, R. P. (1994). The determination of interplanetary magnetic field polarities around sector boundaries using E ¿ 2 keV electrons. *Geophysical Research Letters*, *21*(15), 1575–1578. https://doi.org/10.1029/94GL01362

Kajdič, P., Blanco-Cano, X., Omidi, N., Rojas-Castillo, D., Sibeck, D. G., & Billingham, L. (2017). Traveling foreshocks and transient foreshock phenomena. *Journal of Geophysical Research: Space Physics*, *122*(9), 9148–9168. https://doi.org/10.1002/2017JA023901

Karlsson, T., Heyner, D., Volwerk, M., Morooka, M., Plaschke, F., Goetz, C., & Hadid, L. (2021). Magnetic holes in the solar wind and magnetosheath near Mercury. *Journal of Geophysical Research: Space Physics*, *126*(5). https://doi.org/10.1029/2020JA028961

Karlsson, T., Kullen, A., Liljeblad, E., Brenning, N., Nilsson, H., Gunell, H., & Hamrin, M. (2015). On the origin of magnetosheath plasmoids and their relation to magnetosheath jets. *Journal of Geophysical Research A: Space Physics*, *120*(9), 7390–7403. https://doi.org/10.1002/2015JA021487

Karlsson, T., Liljeblad, E., Kullen, A., Raines, J. M., Slavin, J. A., & Sundberg, T. (2016). Isolated magnetic field structures in Mercury's magnetosheath as possible analogues for terrestrial magnetosheath plasmoids and jets. *Planetary and Space Science*, *129*, 61–73. https://doi.org/10.1016/j.pss.2016.06.002

Keika, K., Nakamura, R., Baumjohann, W., Angelopoulos, V., Kabin, K., Glassmeier, K. H., et al. (2009). Deformation and evolution of solar wind discontinuities through their interactions with the Earths bow shock. *Journal of Geophysical Research*, *114*(9). https://doi.org/10.1029/2008JA013481

Khotyaintsev, Y. V., Graham, D. B., Norgren, C., & Vaivads, A. (2019). Collisionless magnetic reconnection and waves: Progress review. *Frontiers in Astronomy and Space Sciences*, *6*, 70. https://doi.org/10.3389/fspas.2019.00070

Kropotina, J. A., Webster, L., Artemyev, A. V., Bykov, A. M., Vainchtein, D. L., & Vasko, I. Y. (2021). Solar wind discontinuity transformation at the bow shock. *The Astrophysical Journal*, *913*(2), 142. https://doi.org/10.3847/1538-4357/abf6c7

Liemohn, M. W., & Welling, D. T. (2016). Ionospheric and solar wind contributions to magnetospheric ion density and temperature throughout the magnetotail. In C. R.Chappell, R. W.Schunk, P. M.Banks, J. L.Burch, & R. M.Thorne (Eds.), *Geophysical monograph series* (pp. 101–114). John Wiley & Sons, Inc. https://doi.org/10.1002/9781119066880.ch8

Lin, Y. (1997). Generation of anomalous flows near the bow shock by its interaction with interplanetary discontinuities. *Journal of Geophysical Research*, *102*(A11), 24265–24281. https://doi.org/10.1029/97JA01989

Madanian, H., Desai, M. I., Schwartz, S. J., Wilson, L. B., Fuselier, S. A., Burch, J. L., et al. (2021). The dynamics of a high Mach number quasi-perpendicular shock: MMS observations. *The Astrophysical Journal*, *908*(1), 40. https://doi.org/10.3847/1538-4357/abcb88

Madanian, H., Halekas, J. S., Mazelle, C. X., Omidi, N., Espley, J. R., Mitchell, D. L., & McFadden, J. P. (2020). Magnetic holes upstream of the Martian bow shock: MAVEN observations. *Journal of Geophysical Research: Space Physics*, *125*(1). https://doi.org/10.1029/2019JA027198

Maynard, N. C., Farrugia, C. J., Burke, W. J., Ober, D. M., Scudder, J. D., Mozer, F. S., et al. (2011). Interactions of the heliospheric current and plasma sheets with the bow shock: Cluster and Polar observations in the magnetosheath. *Journal of Geophysical Research*, *116*(1). https://doi.org/10.1029/2010JA015872

Maynard, N. C., Farrugia, C. J., Ober, D. M., Burke, W. J., Dunlop, M., Mozer, F. S., et al. (2008). Cluster observations of fast shocks in the magnetosheath launched as a tangential discontinuity with a pressure increase crossed the bow shock. *Journal of Geophysical Research*, *113*(10). https://doi.org/10.1029/2008JA013121

McFadden, J. P., Carlson, C. W., Larson, D., Ludlam, M., Abiad, R., Elliott, B., et al. (2008). The THEMIS ESA plasma instrument and in-flight calibration. *Space Science Reviews*, *141*(1–4), 277–302. https://doi.org/10.1007/s11214-008-9440-2

Mistry, R., Eastwood, J. P., Phan, T. D., & Hietala, H. (2015). Development of bifurcated current sheets in solar wind reconnection exhausts. *Geophysical Research Letters*, *42*(24). https://doi.org/10.1002/2015GL066820

Osman, K. T., Matthaeus, W. H., Gosling, J. T., Greco, A., Servidio, S., Hnat, B., et al. (2014). Magnetic reconnection and intermittent turbulence in the solar wind. *Physical Review Letters*, *112*(21), 215002. https://doi.org/10.1103/PhysRevLett.112.215002

Parker, E. N. (1957). Sweet's mechanism for merging magnetic fields in conducting fluids. *Journal of Geophysical Research*, *62*(4), 509–520. https://doi.org/10.1029/jz062i004p00509

Paschmann, G., Haerendel, G., Papamastorakis, I., Sckopke, N., Bame, S. J., Gosling, J. T., & Russell, C. T. (1982). Plasma and magnetic field characteristics of magnetic flux transfer events. *Journal of Geophysical Research*, *87*(A4), 2159. https://doi.org/10.1029/JA087iA04p02159

Paschmann, G., Øieroset, M., & Phan, T. (2013). In-situ observations of reconnection in space. *Space Science Reviews*, *178*(2–4), 385–417. https://doi.org/10.1007/s11214-012-9957-2

Petrukovich, A. A., & Chugunova, O. M. (2021). Detailed structure of very high-β Earth bow shock. *Journal of Geophysical Research: Space Physics*, *126*(8). https://doi.org/10.1029/2020JA029004

Petschek, H. E. (1964). Magnetic field annihilation. In *The physics of solar flares, proceedings of the AAS-NASA symposium 50* (p. 425).

Phan, T. D., Gosling, J. T., & Davis, M. S. (2009). Prevalence of extended reconnection X-lines in the solar wind at 1 AU. *Geophysical Research Letters*, *36*(9), L09108. https://doi.org/10.1029/2009GL037713

Phan, T. D., Gosling, J. T., Davis, M. S., Skoug, R. M., Øieroset, M., Lin, R. P., et al. (2006). A magnetic reconnection X-line extending more than 390 Earth radii in the solar wind. *Nature*, *439*(7073), 175–178. https://doi.org/10.1038/nature04393

Phan, T. D., Gosling, J. T., Paschmann, G., Pasma, C., Drake, J. F., Øieroset, M., et al. (2010). The dependence of magnetic reconnection on plasma β and magnetic shear: Evidence from solar wind observations. *Astrophysical Journal Letters*, *719*(2 PART 2), L199–L203. https://doi.org/10.1088/2041-8205/719/2/L199

Phan, T. D., Love, T. E., Gosling, J. T., Paschmann, G., Eastwood, J. P., Oieroset, M., et al. (2011). Triggering of magnetic reconnection in a magnetosheath current sheet due to compression against the magnetopause. *Geophysical Research Letters*, *38*(17). https://doi.org/10.1029/2011GL048586

Phan, T. D., Paschmann, G., Twitty, C., Mozer, F. S., Gosling, J. T., Eastwood, J. P., et al. (2007). Evidence for magnetic reconnection initiated in the magnetosheath. *Geophysical Research Letters*, *34*(14), L14104. https://doi.org/10.1029/2007GL030343

Plaschke, F., Hietala, H., & Angelopoulos, V. (2013). Anti-sunward high-speed jets in the subsolar magnetosheath. *Annales Geophysicae*, *31*(10), 1877–1889. https://doi.org/10.5194/angeo-31-1877-2013

Pollock, C., Moore, T., Jacques, A., Burch, J., Gliese, U., Saito, Y., et al. (2016). Fast plasma investigation for magnetospheric multiscale. *Space Science Reviews*, *199*(1–4), 331–406. https://doi.org/10.1007/s11214-016-0245-4

Russell, C. T., Anderson, B. J., Baumjohann, W., Bromund, K. R., Dearborn, D., Fischer, D., et al. (2016). *The magnetospheric multiscale magnetometers* (Vol. 199, No. 1–4). Springer Netherlands. https://doi.org/10.1007/s11214-014-0057-3

Šafránková, J., Němeček, Z., Přech, L., Samsonov, A. A., Koval, A., & Andréeová, K. (2007). Modification of interplanetary shocks near the bow shock and through the magnetosheath. *Journal of Geophysical Research*, *112*(8). https://doi.org/10.1029/2007JA012503

Scholer, M., & Burgess, D. (1992). The role of upstream waves in supercritical quasi-parallel shock re-formation. *Journal of Geophysical Research*, *97*(A6), 8319. https://doi.org/10.1029/92JA00312

Shue, J.-H., Song, P., Russell, C. T., Steinberg, J. T., Chao, J. K., Zastenker, G., et al. (1998). Magnetopause location under extreme solar wind conditions. *Journal of Geophysical Research*, *103*(A8), 17691–17700. https://doi.org/10.1029/98ja01103

Sperveslage, K., Neubauer, F. M., Baumgärtel, K., & Ness, N. F. (2000). Magnetic holes in the solar wind between 0.3 AU and 17 AU. *Nonlinear Processes in Geophysics*, *7*(3/4), 191–200. https://doi.org/10.5194/npg-7-191-2000

Spreiter, J. R., Summers, A. L., & Alksne, A. Y. (1966). Hydromagnetic flow around the magnetosphere. *Planetary and Space Science*, *14*(3), 223–253. https://doi.org/10.1016/0032-0633(66)90124-3

Stone, E. C., Frandsen, A. M., Mewaldt, R. A., Christian, E. R., Margolies, D., Ormes, J. F., & Snow, F. (1998). The advanced composition explorer. *Space Science Reviews*, *86*(1–4), 1–22. https://doi.org/10.1007/978-94-011-4762-0_1

Trattner, K. J., Burch, J. L., Ergun, R., Fuselier, S. A., Gomez, R. G., Grimes, E. W., et al. (2016). The response time of the magnetopause reconnection location to changes in the solar wind: MMS case study. *Geophysical Research Letters*, *43*(10), 4673–4682. https://doi.org/10.1002/2016GL068554

Trattner, K. J., Burch, J. L., Fuselier, S. A., Petrinec, S. M., & Vines, S. K. (2020). The 18 November 2015 magnetopause crossing: The GEM dayside kinetic challenge event observed by MMS/HPCA. *Journal of Geophysical Research: Space Physics*, *125*(7). https://doi.org/10.1029/2019JA027617

Trattner, K. J., Mulcock, J. S., Petrinec, S. M., & Fuselier, S. A. (2007). Probing the boundary between antiparallel and component reconnection during southward interplanetary magnetic field conditions. *Journal of Geophysical Research*, *112*(8). https://doi.org/10.1029/2007JA012270

Treumann, R. A., & Baumjohann, W. (2013). Collisionless magnetic reconnection in space plasmas. *Frontiers in Physics*, *1*. https://doi.org/10.3389/fphy.2013.00031

Tsurutani, B. T., Lakhina, G. S., Verkhoglyadova, O. P., Echer, E., Guarnieri, F. L., Narita, Y., & Constantinescu, D. O. (2011). Magnetosheath and heliosheath mirror mode structures, interplanetary magnetic decreases, and linear magnetic decreases: Differences and distinguishing features. *Journal of Geophysical Research*, *116*(2). https://doi.org/10.1029/2010JA015913

Turc, L., Escoubet, C. P., Fontaine, D., Kilpua, E. K., & Enestam, S. (2016). Cone angle control of the interaction of magnetic clouds with the Earth's bow shock. *Geophysical Research Letters*, *43*(10), 4781–4789. https://doi.org/10.1002/2016GL068818

Turc, L., Tarvus, V., Dimmock, A. P., Battarbee, M., Ganse, U., Johlander, A., et al. (2020). Asymmetries in the Earth's dayside magnetosheath: Results from global hybrid-Vlasov simulations. *Annales Geophysicae*, *38*(5), 1045–1062. https://doi.org/10.5194/angeo-38-1045-2020

Turner, J. M., Burlaga, L. F., Ness, N. F., & Lemaire, J. F. (1977). Magnetic holes in the solar wind. *Journal of Geophysical Research*, *82*(13), 1921–1924. https://doi.org/10.1029/ja082i013p01921

Volwerk, M., Mautner, D., Simon Wedlund, C., Goetz, C., Plaschke, F., Karlsson, T., et al. (2021). Statistical study of linear magnetic hole structures near Earth. *Annales Geophysicae*, *39*(1), 239–253. https://doi.org/10.5194/angeo-39-239-2021

Wang, G. Q., Volwerk, M., Xiao, S. D., Wu, M. Y., Hao, Y. F., Liu, L. J., et al. (2020). Three-dimensional geometry of the electron-scale magnetic hole in the solar wind. *The Astrophysical Journal Letters*, *904*(1), L11. https://doi.org/10.3847/2041-8213/abc553

Webster, L., Vainchtein, D., & Artemyev, A. (2021). Solar wind discontinuity interaction with the bow shock: Current density growth and dawn-dusk asymmetry. *Solar Physics*, *296*(6), 87. https://doi.org/10.1007/s11207-021-01824-2

Yamada, M., Kulsrud, R., & Ji, H. (2010). Magnetic reconnection. *Reviews of Modern Physics*, *82*(1), 603–664. https://doi.org/10.1103/RevModPhys.82.603

Yao, S. T., Wang, X. G., Shi, Q. Q., Pitkänen, T., Hamrin, M., Yao, Z. H., et al. (2017). Observations of kinetic-size magnetic holes in the magnetosheath. *Journal of Geophysical Research: Space Physics*, *122*(2), 1990–2000. https://doi.org/10.1002/2016JA023858

Zhang, H., Zong, Q. G., Sibeck, D. G., Fritz, T. A., McFadden, J. P., Glassmeier, K. H., & Larson, D. (2009). Dynamic motion of the bow shock and the magnetopause observed by THEMIS spacecraft. *Journal of Geophysical Research*, *114*(1). https://doi.org/10.1029/2008JA013488

Zweibel, E. G., & Yamada, M. (2016). Perspectives on magnetic reconnection. *Proceedings of the Royal Society A: Mathematical, Physical & Engineering Sciences*, *472*(2196), 20160479. https://doi.org/10.1098/rspa.2016.0479